Solid Polymer Electrolytes with Enhanced Electrochemical Stability for High-Capacity Aluminum Batteries

*Oi Man Leung, Leo W. Gordon, Robert J. Messinger, Themis Prodromakis, Julian A. Wharton, Carlos Ponce de León, and Theresa Schoetz**

Chloroaluminate ionic liquids are commonly used electrolytes in rechargeable aluminum batteries due to their ability to reversibly electrodeposit aluminum at room temperature. Progress in aluminum batteries is currently hindered by the limited electrochemical stability, corrosivity, and moisture sensitivity of these ionic liquids. Here, a solid polymer electrolyte based on 1-ethyl-3-methylimidazolium chloride-aluminum chloride, polyethylene oxide, and fumed silica is developed, exhibiting increased electrochemical stability over the ionic liquid while maintaining a high ionic conductivity of ≈ 13 mS cm^{-1}. In aluminum–graphite cells, the solid polymer electrolytes enable charging to 2.8 V, achieving a maximum specific capacity of 194 mA h g^{-1} at 66 mA g^{-1}. Long-term cycling at 2.7 V showed a reversible capacity of 123 mA h g^{-1} at 360 mA g^{-1} and 98.4% coulombic efficiency after 1000 cycles. Solid-state nuclear magnetic resonance spectroscopy measurements reveal the formation of five-coordinate aluminum species that crosslink the polymer network to enable a high ionic liquid loading in the solid electrolyte. This study provides new insights into the molecular-level design and understanding of polymer electrolytes for high-capacity aluminum batteries with extended potential limits.

1. Introduction

Electrochemical energy storage devices are indispensable to modern society, having a plethora of uses in wide-ranging applications. Rechargeable Al batteries have been explored as potential next-generation energy storage devices owing to the natural abundance of Al in the Earth's crust (8.1 wt%, compared to 0.002 wt% for Li) and its desirable electrochemical properties. An Al negative electrode has a theoretical specific capacity

of 2980 mA h g^{-1} (vs 3860 mA h g^{-1} of Li),[1] while its theoretical volumetric capacity of 8040 mA h cm^{-3} is almost four times that of Li, due to the three electrons transferred during the charge and discharge processes. The stability of Al in air and the wide availability of non-flammable electrolytes also present significant advantages in terms of inherent safety, which are crucial to many battery applications.

A variety of aqueous and non-aqueous electrolytes have been investigated, ranging from inorganic molten salts,[2] deep eutectic solvents,[3,4] water-in-salt electrolytes[5,6] and ionic liquids,[7–9] to gel and solid polymer electrolytes.[10–14] Of these, the most commonly researched system consists of a graphite positive electrode and an Al metal negative electrode paired with Lewis acidic melts of the 1-ethyl-3-methylimidazolium chloride-aluminum chloride ionic liquid (EMImCl-AlCl$_3$), where the molar ratio of AlCl$_3$ to EMImCl is >1. The operating mechanism of an Al–graphite cell involves the reversible intercalation of AlCl$_4^-$ anions into the graphite positive electrode and the simultaneous electrodeposition and stripping of metallic Al at the negative electrode, involving both Al$_2$Cl$_7^-$ and AlCl$_4^-$ anions that originate from the electrolyte. The balance between these chloroaluminate species must therefore be optimized for further improvements in electrochemical performance. Currently, the empirical specific capacities of Al–natural graphite cells with EMImCl-AlCl$_3$ ionic

O. M. Leung, J. A. Wharton, C. Ponce de León, T. Schoetz
Faculty of Engineering and Physical Sciences
University of Southampton
Southampton SO17 1BJ, UK
E-mail: schoetz@illinois.edu

L. W. Gordon, R. J. Messinger, T. Schoetz
Department of Chemical Engineering
The City College of New York
CUNY
New York 10031, USA

T. Prodromakis
Centre for Electronics Frontiers
School of Engineering
University of Edinburgh
Edinburgh EH9 3JL, UK

T. Schoetz
Chemical and Biomolecular Engineering
University of Illinois at Urbana-Champaign
Urbana, IL 61801, USA

liquid electrolytes range between 60 and 150 mA h g^{-1}[7,9,15,16], far from the estimated theoretical specific capacity of 240 mA h g^{-1} for fully intercalated graphite.[17] In part, this deficit in specific capacity is due to the narrow electrolyte potential stability window, which limits the upper cut-off potential to ≈2.45 V.[1,17]

Recently, the development of polymer-based electrolytes has been incentivized by a growing interest in solid-state energy storage technologies. Electrolytes in a solid or gel state can mitigate the risk of electrolyte leakage and eliminate the need for a glass-fiber separator that restricts electrolyte utilization[18,19] and contributes to the non-active weight of the battery.[10,11,20] A number of different approaches have been taken to synthesize polymer electrolytes for Al batteries, including in situ polymerization of monomers in EMImCl-AlCl$_3$[11,13,18] and Et$_3$NHCl-AlCl$_3$,[10,19] as well as the direct mixing of a polymer host with ionic liquids and deep eutectic solvents via solvent-free processes.[10,12,21,22] Electrolytes polymerized in situ have demonstrated improved resistance to moisture and performed well under mechanical flexion,[19,23] while solvent-free synthesis methods can help avoid unwanted side reactions with the strongly electrophilic Al$_2$Cl$_7^-$ ions, which tend to react and form complexes with functional groups containing lone electrons, resulting in a loss of electrochemical activity.[13,24–26] Further benefits of incorporating a polymer matrix to encapsulate the liquid phase include the possibility of widening the electrolyte potential stability window.[12,18,27,28]

In our previous investigation involving ionogels formed by dissolving polyethylene oxide (PEO) in Lewis neutral melts of the EMImCl-AlCl$_3$ ionic liquid (AlCl$_3$/EMImCl molar ratio = 1), the improvement in potential stability enabled the electrodeposition of small amounts of Al from the ionogel.[12] This is not observed from neat mixtures of the Lewis neutral ionic liquid, as the electrochemical reduction of its constituent chloroaluminate anions, AlCl$_4^-$, to metallic Al, typically occurs at a lower potential than its cathodic stability limit at ≈−0.6 V vs Al|Al(III). However, the coulombic efficiency of Al deposition remained low (≈60%) due to the very low AlCl$_4^-$ diffusion coefficient (1.03 × 10^{-18} m^2 s^{-1}). Improvements to the transport properties may be made through the addition of plasticizers such as inorganic particles since the movement of ions in polymer electrolytes typically occurs in the amorphous phase of semi-crystalline polymers. Although these additions have been shown to reduce the crystallinity of polymers to provide a high-entropy medium for ion transport and promote the ionic conductivity of electrolytes in various multivalent metal-ion battery systems,[29–31] their effects have yet to be studied in Al battery applications. Additionally, despite several reports of electrolytes exhibiting enhanced electrochemical stabilities, long-term cycling at elevated charging potentials has rarely been demonstrated in Al–graphite batteries.

Herein, we present a new solid polymer electrolyte based on a Lewis acidic EMImCl-AlCl$_3$ ionic liquid, PEO, and fumed silicon dioxide (SiO$_2$) as an additive, synthesized through a solvent-free method. The polymer electrolyte shows significantly increased potential stabilities over the neat ionic liquid, which enables charging of Al–natural graphite cells to upper cut-off potentials of up to 2.8 V and improves on the specific capacities currently achieved with conventional ionic liquid electrolytes by ≈30%. The individual and synergistic effects of PEO and SiO$_2$ within the polymer electrolytes are investigated via electrochemical and spectroscopic techniques, including variable-rate cyclic

voltammetry, electrochemical impedance spectroscopy (EIS), galvanostatic cycling and solid-state nuclear magnetic resonance (NMR) spectroscopy. The optimized polymer electrolyte composition exhibits a high ionic conductivity of 13.2 mS cm^{-1}, allowing for highly reversible cycling at elevated charge-discharge rates up to 2 A g^{-1}, and demonstrates a stable and long cycling lifetime of over 1000 cycles at 2.7 V.

2. Results and Discussion

2.1. Al Electrodeposition in Polymer Electrolytes

To demonstrate the electrochemical feasibility of using the solid polymer electrolytes in Al batteries, the reversible electrodeposition of Al metal in the electrolytes was first investigated in a three-electrode cell using glassy carbon working and counter electrodes. Cyclic voltammograms (CVs) of the polymer electrolytes containing up to 7 wt% PEO display a profile typical of reversible Al metal electrodeposition, with a characteristic nucleation loop commonly observed during the electrodeposition of metal films on foreign substrates. The crossover of the current associated with the forward and reverse scans occurs due to the activation energy required for the initial nucleation on the glassy carbon electrode. A minimum of 4 wt% PEO was required to induce solidification of the polymer electrolyte mixtures; as such, compositions with <4 wt% PEO were not considered in this study. The polymer electrolytes (PE) are referred to as PE-x-y, where x and y are the respective weight percentages of PEO and fumed SiO$_2$. The current densities of the electrodeposition peaks range between −8 and −3 mA cm^{-2} at a scan rate of 20 mV s^{-1} (Figure S1a, Supporting Information) and a CV of the PE-6-0.5 electrolyte is shown in **Figure 1**a, where redox peaks corresponding to the deposition and dissolution of Al from Al$_2$Cl$_7^-$ anions (Equation (1)) are observed at −0.23 and 0.02 V vs Al|Al(III) respectively:

$$4Al_2Cl_7^- + 3e^- \rightleftharpoons Al + 7AlCl_4^- \tag{1}$$

The magnitudes of the anodic and cathodic current densities were found to drop significantly in electrolytes containing beyond 7 wt% PEO. The respective peak current densities of electrodeposition and dissolution of the PE-8-0 electrolyte are 0.07 mA cm^{-2} and −0.15 mA cm^{-2}, which are ≈95% lower than those of the PE-7-0 electrolyte. At 10 wt% PEO, no redox peaks appear in the range of −0.5 to 1.0 V vs Al|Al(III) (see Figure S1a, Supporting Information, inset). The decrease and eventual loss of electrochemical activity at higher amounts of PEO are likely caused by the crosslinking and simultaneous consumption of Al$_2$Cl$_7^-$ ions with PEO chains, which is discussed in greater detail below.

Developing electrolytes with a wide electrochemical stability window is key to further improving the performance of Al batteries since this allows for higher charging cut-off potentials, leading to increased capacity. Incorporating PEO in Lewis neutral EMImCl-AlCl$_3$ ionic liquids (AlCl$_3$/EMImCl molar ratio = 1) has previously demonstrated improvements to the electrochemical stability window by up to 1 V.[12] Here, a similar effect was observed in polymer electrolytes based on Lewis acidic compositions, which show enhanced potential stability in both the
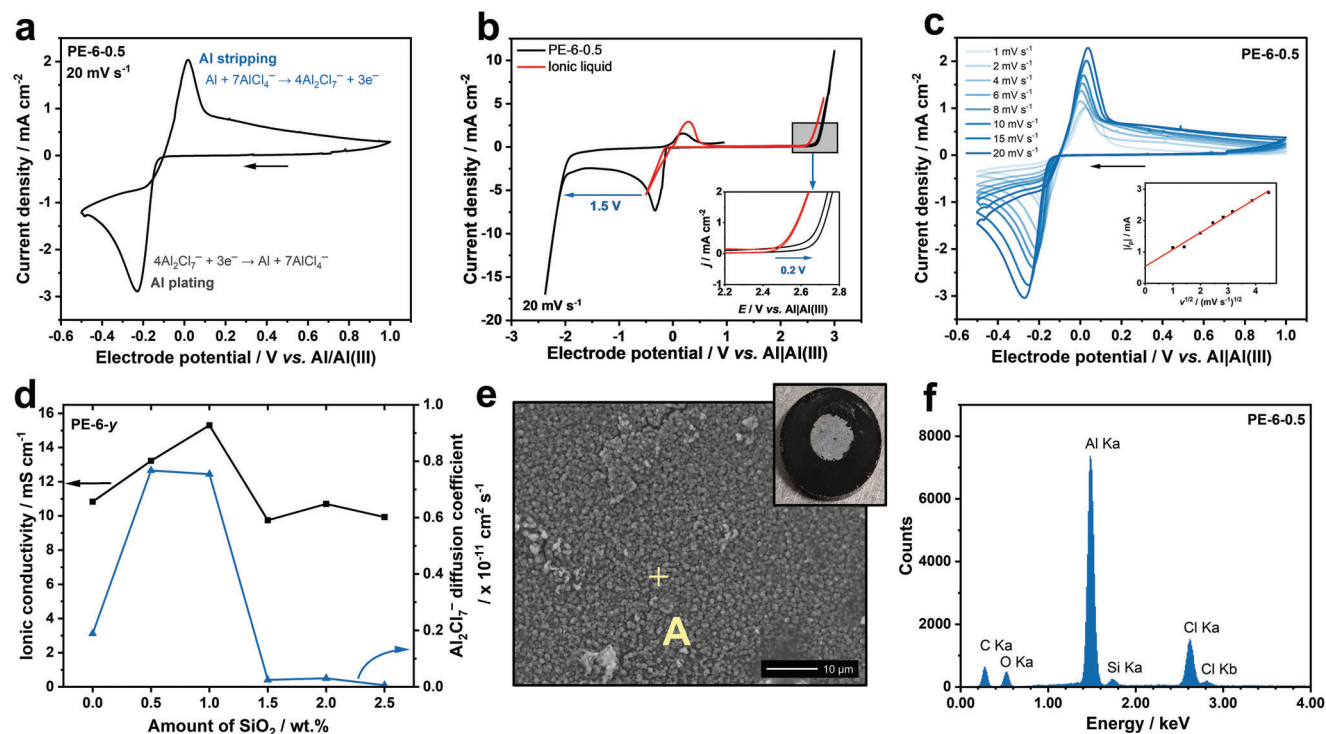
Figure 1. CVs showing: a) the Al plating and stripping reactions of the PE-6-0.5 electrolyte, b) the potential stability windows of neat EMImCl-AlCl$_3$ and PE-6-0.5, and c) reversible Al electrodeposition from the PE-6-0.5 electrolyte, measured at various scan rates in a three-electrode cell. The inset figure in c) shows a plot of the magnitude of the peak cathodic current versus the square root of the scan rate. d) Ionic conductivities and Al$_2$Cl$_7^-$ diffusion coefficients of PE-6-y electrolytes containing varying amounts of fumed SiO$_2$. e) SEM of electrodeposited Al on glassy carbon, obtained from PE-6-0.5 by applying a constant potential of −0.3 V vs Al|Al(III) for 30 min. The inset figure shows a photograph of the electrodeposited Al film on glassy carbon. f) EDX spectrum corresponding to the point marked "A" in (e).

cathodic and anodic directions as investigated via cyclic voltammetry in a three-electrode cell (Figure 1b). The stability limits were quantified though linear regression of the CV curves prior to and after the onset of electrolyte decomposition (Figure 1b, inset), taking the point of intersection of the two linear fits as the stability limit.[32] Full details of the calculation methods and electrochemical stability ranges of polymer electrolyte samples investigated in this paper are provided in Figure S2, and Tables S1 and S2 (Supporting Information). The PE-6-1 electrolyte exhibited the widest potential stability window, ranging between −2.12 V and 2.77 V vs Al|Al(III), representing a 9% increase in the anodic stability limit over the neat ionic liquid. In practical Al−graphite cells with EMImCl-AlCl$_3$ ionic liquid electrolytes, the onset of AlCl$_4^-$ oxidation and the accompanying evolution of chlorine gas begins to occur after ≈2.45 V due to the high surface area of the graphite electrode.[1,33–35] The cathodic limit is bounded by the reduction of the organic EMIm$^+$ cation to EMIm.[36] These improvements in stability are not thermodynamic in nature and may be attributed to the increase in the relative permittivity (dielectric constant) of the resulting polymer electrolyte upon the addition of PEO, which decreases the effective potential to an extent such that a larger overpotential is required to achieve the same current.[12]

The ion transport properties of the polymer electrolytes in relation to their Al electrodeposition performance were subsequently probed by evaluating their ionic conductivities and Al$_2$Cl$_7^-$ diffusion coefficients. The ionic conductivities of the electrolytes were

determined by EIS in a three-electrode cell using the ohmic resistance, taken as the intercept of the real axis of the complex plane plot (Equation S1, Supporting Information). Figure 1d and Figure S3 (Supporting Information) show ionic conductivities of the polymer electrolytes as a function of SiO$_2$ and PEO content, ranging from 6.25 mS cm^{-1} (PE-7-0) to 15.3 mS cm^{-1} (PE-6-1). These values are in the same order of magnitude as the EMImCl-AlCl$_3$ ionic liquid (≈19 mS cm^{-1}[37,38]) and are comparatively higher than most other Al battery polymer electrolytes reported in the literature (0.25–6.61 mS cm^{-1}),[10,11,18–20,27,28,39,40] owing to the high loading of ionic liquid within the electrolyte, at over 93 wt%. Similarly high ionic conductivities have been reported in polymer electrolytes with comparable ionic liquid loadings.[23] Complex plane and Bode plots of the impedance spectra obtained from the PE-6-y electrolytes are shown in Figure S4 (Supporting Information).

To determine the diffusion coefficients of the electroactive Al$_2$Cl$_7^-$ species that is responsible for Al electrodeposition, variable-rate cyclic voltammetry was performed at scan rates ranging from 1 to 20 mV s^{-1}, shown in Figure 1c and Figure S5 (Supporting Information). For faradaic diffusion-limited processes such as the deposition of metallic Al,[41] plotting the peak cathodic current, i_p, corresponding to Al electrodeposition against the square root of the scan rate, $v^{1/2}$, yields a linear curve (inset of Figure 1c; Figure S5d–f,j–l, Supporting Information), from which the slope can be used to determine the diffusion coefficient using the Randles–Ševčík equation (Equation S2,

Supporting Information). The diffusion coefficients of $Al_2Cl_7^-$ decrease with increasing amounts of PEO due to the restricted ion mobility associated with encapsulating the ionic liquid in the polymer matrix (Figure S3, Supporting Information). Note that while the ionic conductivities and $Al_2Cl_7^-$ diffusion coefficients of the PE-6-γ polymer electrolytes in Figure 1d follow a similar trend, the $Al_2Cl_7^-$ diffusion coefficients of the PE-x–0 polymer electrolytes containing 4, 5 and 6 wt% PEO decrease with greater amounts of PEO, despite a modest increase in ionic conductivity. Since the molar concentrations of $Al_2Cl_7^-$ used to compute its diffusion coefficients in each polymer electrolyte were scaled based on its concentration in neat EMImCl-AlCl$_3$, the actual concentrations of $Al_2Cl_7^-$ in the polymer electrolytes are likely lower than the calculated values, given the interactions (and thus consumption, as discussed below) of the $Al_2Cl_7^-$ species with the PEO chains. This results in diffusion coefficients that are lower than the actual values, explaining the discrepancies between the trends observed.

Al electrodeposition from the polymer electrolytes was further investigated qualitatively by evaluating the morphologies of electrodeposited Al on glassy carbon substrates via scanning electron microscopy (SEM). A constant potential of −0.3 V vs Al|Al(III) was applied to the three-electrode cell for 30 min, yielding light grey Al films (Figure 1e, inset). The Al deposits were rinsed with dimethyl carbonate following electrodeposition to remove the electrolyte on the surface prior to SEM and energy-dispersive X-ray (EDX) analyses. The electrodeposits obtained from the PE-6-0.5 electrolyte (Figure 1e) are dense, generally spherical, and relatively uniform in size, ranging between 0.85 and 1.1 μm. The corresponding EDX spectrum in Figure 1f confirms the purity of the deposits, as the only signals additional to Al are O, C, Cl, and Si, from the glassy carbon substrate and the remaining electrolyte residue. Micrographs of deposits obtained from other electrolyte compositions are shown in Figure S6a–d (Supporting Information), with their corresponding EDX spectra in Figure S7a–d (Supporting Information). The formation of dendrites, which would be detrimental to the longevity of the battery, was not evident in any of the electrodeposited Al films due to the low steady-state current density during electrodeposition (<1 mA cm^{-2}). In pure EMImCl-AlCl$_3$, the growth of dendrites is typically only observed at current densities above 40 mA cm^{-2}.[42]

2.2. Molecular-Level Understanding of Electrolyte Properties by Solid-State Nuclear Magnetic Resonance (NMR) Spectroscopy

The chloroaluminate ion speciation within the polymer electrolyte and molecular-level origins of the solidification process were studied by solid-state ^{27}Al, ^{29}Si and ^{1}H NMR spectroscopy. Solid-state ^{27}Al single-pulse magic-angle-spinning (MAS) spectra were acquired under quantitative conditions on the PE-6-0 and PE-6-0.5 polymer electrolytes (**Figure 2a,b**). As expected, the chloroaluminate species $AlCl_4^-$ and $Al_2Cl_7^-$ were observed at 103.2 and 97.4 ppm, respectively.[37] Notably, an additional ^{27}Al signal was present at ≈50 ppm, whose ^{27}Al shift indicates that it is associated with Al in a five-coordinate Al environment. This Al environment, which only represents a small molar fraction of the overall Al atoms, was hypothesized to be associated with PEO crosslinking sites.

To test this hypothesis, a $^{27}Al\{^{1}H\}$ dipolar-mediated heteronuclear multiple-quantum coherence (D-HMQC) NMR experiment was performed (Figure 2c), which yields signals only from ^{27}Al nuclei that are dipole-dipole coupled (through-space) to ^{1}H nuclei. The NMR experiment thus acts a dipolar-mediated filter, detecting Al that (*i*) are in close molecular proximity (<1 nm) to protons, while (*ii*) both nuclei must remain relatively immobile (fast, isotropic mobility averages dipolar couplings to zero). Interestingly, the $^{27}Al\{^{1}H\}$ D-HMQC NMR spectrum reveals significant ^{27}Al signal intensity from the five-coordinate Al moieties at 50 ppm, indicating that these five-coordinate species interact through-space with molecularly proximate protons and are relatively immobile. As the EMIm$^+$ cations are mobile and liquid-like, these protons must be associated with the PEO chains. Note that some ^{27}Al signals associated with $AlCl_4^-$ anions also appear in the spectrum, indicating that a population interacts with the PEO chains. To understand which protons these Al species are interacting with, a 2D $^{27}Al\{^{1}H\}$ D-HMQC NMR experiment was performed (Figure 2d), which reveals interactions between ^{27}Al signals associated with both $AlCl_4^-$ and the five-coordinate Al moieties and broad ^{1}H signal intensity spanning from ≈−1 to 6 ppm. The ^{1}H species that interact with the ^{27}Al species exhibit lower ^{1}H chemical shifts (maximum at 2.4 ppm) relative to pristine PEO (^{1}H CH$_2$ at 3.4 ppm), likely due to the locally reduced electron density of the adjacent oxygen atoms at the crosslinking sites that would have a drastic impact on the electrolyte's mechanical properties.

A 2D $^{27}Al\{^{27}Al\}$ multiple-quantum-MAS (MQ-MAS) experiment was also performed to probe the quadrupolar nature of the five-coordinate Al species (Figure 2e). The fit of this ^{27}Al quadrupolar lineshape (red) yielded a quadrupolar coupling constant (C_Q) of 5.82 MHz and a quadrupolar asymmetry parameter (η_Q) of 0.85. Density functional theory (DFT) calculations to obtain quadrupolar NMR parameters of the five-coordinate $AlCl_xO_y$ species established $AlCl_3O_2$ as the most likely candidate (Table S3, Supporting Information). In aggregate, the solid-state NMR and DFT results suggest that $Al_2Cl_7^-$ reacts with the lone electron-bearing oxygen atoms of the ethylene oxide units of two PEO chains to form a crosslinked structure that results in its solidification (Figure 2f) through the process described in Equation (2):

$$Al_2Cl_7^- + 2\left(OCH_2CH_2\right) \rightarrow AlCl_4^- + AlCl_3 \cdot 2\left(OCH_2CH_2\right) \qquad (2)$$
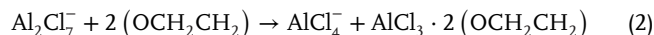
The role of $Al_2Cl_7^-$ in the solidification process is further evidenced by the fact that Lewis neutral PEO-EMImCl-AlCl$_3$ ionogels remain as a viscous liquid and do not solidify over time, since they do not contain $Al_2Cl_7^-$ ions.[12] As expected, the integrated ^{27}Al signal intensities corresponding to $Al_2Cl_7^-$ decrease relative to $AlCl_4^-$ upon the addition of PEO. The $Al_2Cl_7^-$:$AlCl_4^-$ molar ratios of neat EMImCl-AlCl$_3$ and PE-6-0 are 1:8.5 to 1:12.8 respectively, indicating a reduction in Lewis acidity arising from the consumption of $Al_2Cl_7^-$ to form the five-coordinate $AlCl_3O_2$ crosslinking moieties. In deep eutectic liquids like AlCl$_3$-urea,[44] the interaction of PEO with $Al_2Cl_7^-$ has been reported to occur via the bonding of AlCl$_3$ with one, rather than two, ethylene oxide unit of the PEO. This observation may also explain why the urea-based polymer electrolytes using PEO of the same molecular weight (100 000 g mol^{-1}) and in similar amounts (5 wt%)

**ADVANCED
SCIENCE NEWS**

www.advancedsciencenews.com

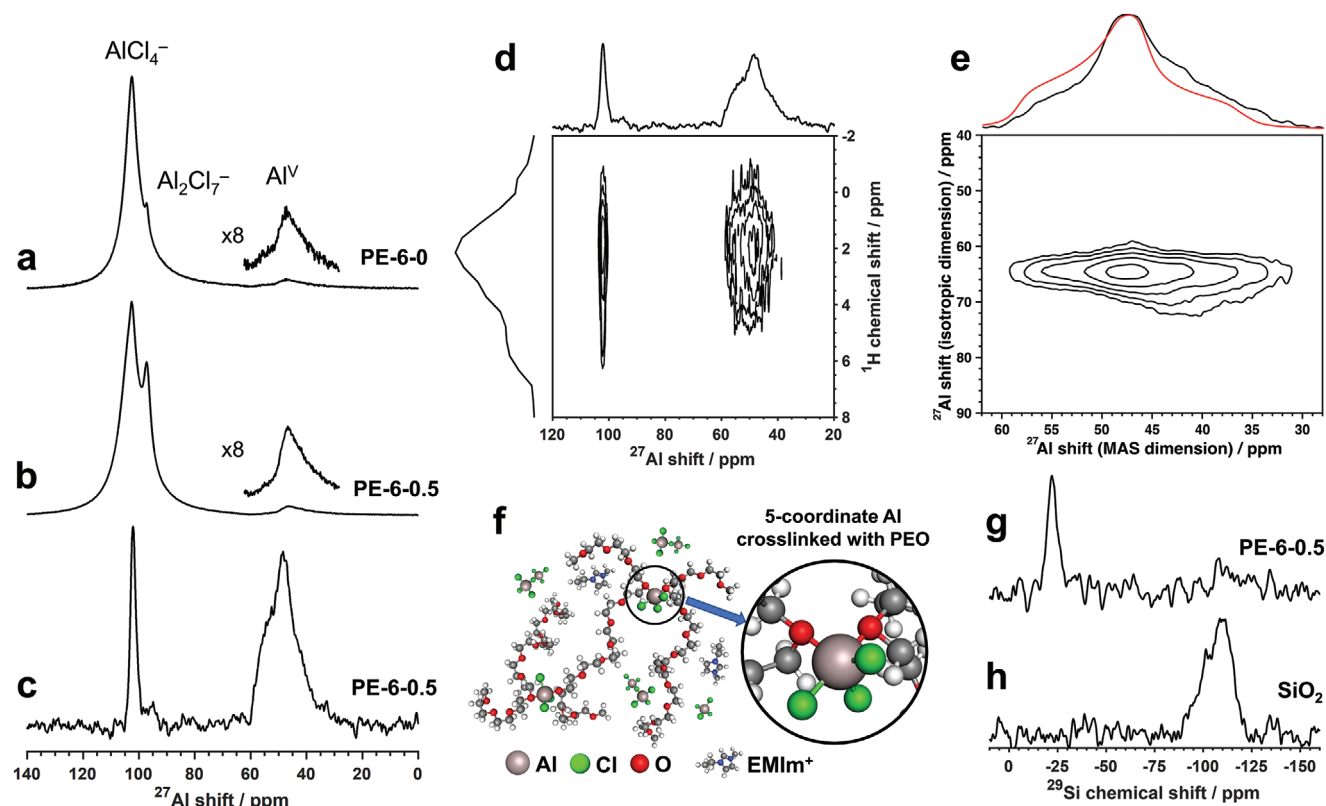**ADVANCED
ENERGY
MATERIALS**

www.advenergymat.de

Figure 2. Solid-state ^{27}Al single-pulse NMR spectra of a) PE-6-0, and b) PE-6-0.5 acquired under quantitative conditions. c) Solid-state ^{27}Al{^{1}H} D-HMQC NMR spectrum of PE-6-0.5. Solid-state d) 2D ^{27}Al{^{1}H} D-HMQC and e) 2D ^{27}Al{^{27}Al} MQ-MAS NMR spectra of PE-6-0.5, with the simulated quadrupolar ^{27}Al lineshape shown in red.[43] f) Schematic of the crosslinked PEO chains within the polymer electrolyte. Solid-state ^{29}Si single-pulse NMR spectra of g) PE-6-0.5, and h) fumed SiO$_2$ acquired under quantitative conditions.

described by Miguel et al.[22] behave as an elastomer and were not reported to solidify like the EMImCl-AlCl$_3$-based electrolytes in this work. The formation of this five-coordinate Al species is crucial to the electrochemical performance of the solid polymer electrolytes, since it allows for a uniquely high loading of the ionic liquid within the solid electrolyte that results in ionic conductivities (>10 mS cm^{-1}) that are comparable with the neat ionic liquid.

Solid-state ^{29}Si NMR measurements were performed to understand the role of fumed SiO$_2$ in PE-6-0.5 (Figure 2g). SiO$_2$ is typically expected to have a broad distribution of ^{29}Si signals centered at ≈−110 ppm that are associated with Q^4 sites (Figure 2h); however, only a single ^{29}Si resonance was detected at ≈−22 ppm in the PE-6-0.5 electrolyte, establishing that SiO$_2$ has reacted in the Lewis acidic polymer electrolyte. After two weeks of aging in the solid-state NMR rotor, the ^{29}Si signal disappeared, while the rotor was found to be pressurized upon opening. The species yielding the ^{29}Si signal at −22 ppm may be a volatile or gaseous species, such as either SiCl$_4$ or another M^0/D^0-site silicon species.

The ratio of the relative ^{27}Al signal intensities of Al$_2$Cl$_7^-$ to AlCl$_4^-$ in the PE-6-0.5 electrolyte was initially found to be ≈1:8.5, changing to 1:2 after two weeks of aging, suggesting that AlCl$_4^-$ is the chloroaluminate reacting with SiO$_2$ (Figure S8, Supporting Information). However, the reaction(s) that occur and the precise molecular nature of the silicon product(s) are left for future investigations. These findings indicate that the mechanisms behind the performance improvements observed upon adding

small amounts (<1 wt%) of fumed SiO$_2$ differ from the typical application of SiO$_2$ in semi-crystalline polymers to increase their amorphicity and thus ion mobility.[45] Rather, SiO$_2$ serves as a sacrificial component that increases the Lewis acidity of the polymer electrolyte to enable higher charge storage capacities.[46,47]

2.3. Understanding the Charge Storage Mechanisms via Variable-Rate Cyclic Voltammetry

The intercalation of AlCl$_4^-$ ions into graphite is a faradaic process during which electrons are transferred at the electrode-electrolyte interface. The faradaic charge storage mechanism can be categorized into two distinct processes: faradaic diffusion-limited, and faradaic non-diffusion-limited (pseudocapacitive) charge storage. Faradaic diffusion-limited charge storage occurs when the rate of electron transfer during the electrochemical redox reaction is significantly faster than the mass transport of ions to the electrode surface.[41] The ultrafast charging and discharging capabilities of Al–graphite batteries with an EMImCl-AlCl$_3$ often reported[7] are attributed to the high pseudocapacitive contributions that enable non-diffusion-limited intercalation of AlCl$_4^-$ anions into graphite. These pseudocapacitive characteristics should therefore be preserved as much as possible when tuning the electrochemical properties of an electrolyte. The respective contributions of (pseudo)capacitive and faradaic diffusion-limited
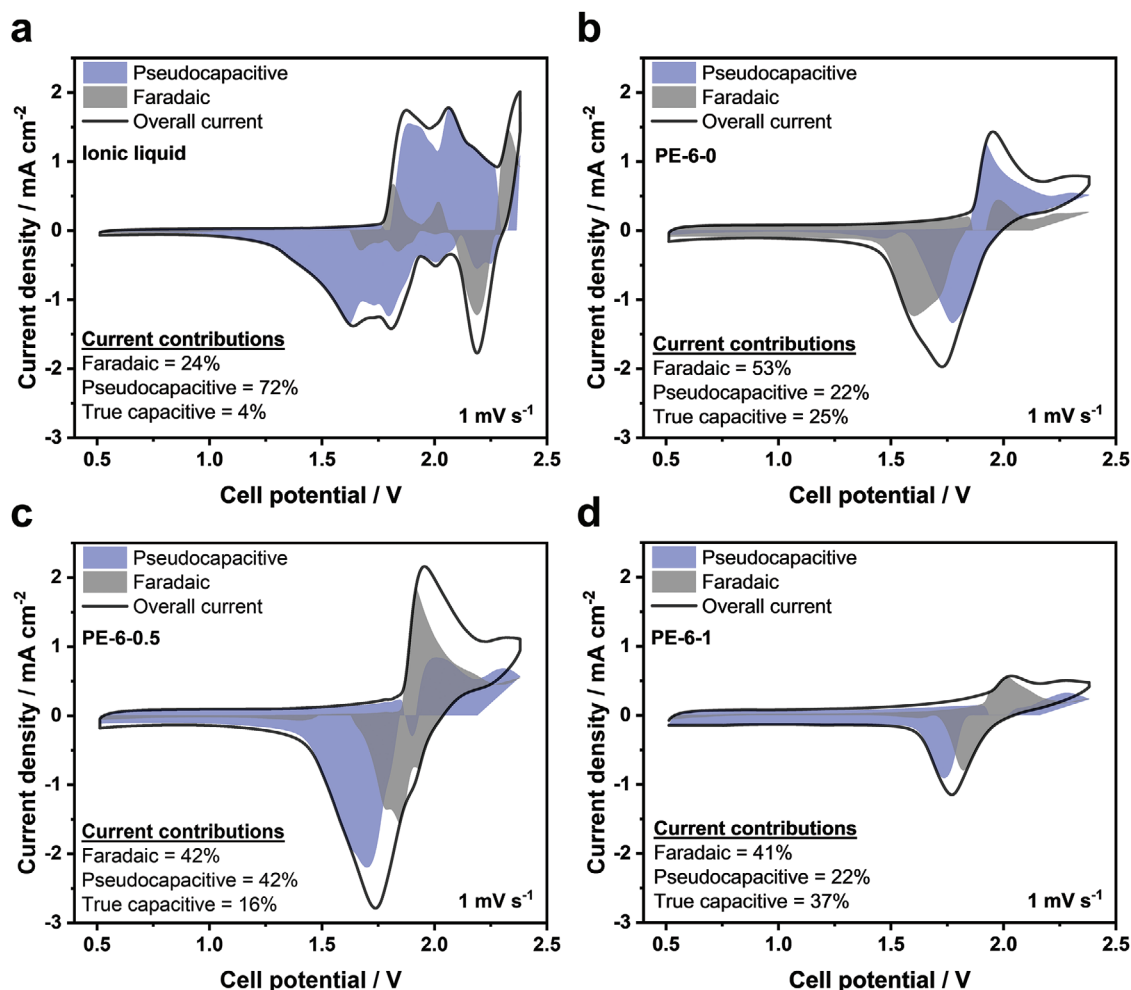
Figure 3. Relative proportions of faradaic, pseudocapacitive and true capacitive current of the overall current for Al–natural graphite cells assembled with: a) neat EMImCl-AlCl$_3$, b) PE-6-0, c) PE-6-0.5, and d) PE-6-1 electrolytes.

current to the total current can be quantified through variable-rate CV analysis, or "Dunn's method", where the contributions of diffusion- and non-diffusion-limited current are assumed to scale linearly with the square root of the scan rate and the scan rate, respectively.

Variable-rate CVs of Al–natural graphite cells assembled with the neat ionic liquid, and PE-6-0, PE-6-0.5, and PE-6-1 electrolytes were recorded at scan rates between 0.1 and 1.0 mV s^{-1} (Figure S9a–d, Supporting Information). The current of each sample was deconvoluted mathematically for the fast scan rate (1 mV s^{-1}) as detailed in ref. [41] to determine the relative proportions of (pseudo)capacitive and faradaic current contributions (**Figure 3**a–d). The (pseudo)capacitive component includes both pseudocapacitive (faradaic non-diffusion limited) and true capacitive current, the latter of which occurs within the electrochemical double layer at the electrode–electrolyte interface, stemming from the physical separation of charges. True capacitive charge storage contributions are typically small in natural graphite electrodes (below 5% of the total current), due to the small specific surface area of graphite compared to the total theoretical inter-

layer surface area.[15,17] Higher true capacitive contributions are, however, observed in the cells assembled with the polymer electrolytes (up to 37% for PE-6-1, see Figure 3d), owing to the low conductivity of PEO and fumed SiO$_2$, which leads to the accumulation of charge at the electrode surface.

In the ionic liquid, AlCl$_4^-$ intercalation into graphite operates in a predominantly pseudocapacitive regime at potentials below 2.3 V. Forming the polymer electrolyte with 6 wt% PEO decreases the pseudocapacitive current to only 22% (Figure 3b), due to the decreased ion mobility. Interestingly, the pseudocapacitive properties are partially recovered upon incorporating 0.5 wt% SiO$_2$ (Figure 3c), although the pseudocapacitive component is again reduced to only 22% in the PE-6-1 electrolyte. The CV of the PE-6-1 electrolyte shows the lowest current density, indicating a slow rate of AlCl$_4^-$ intercalation. PE-6-0.5 is expected to exhibit the best fast-charging performance of the three polymer electrolyte samples, although the ionic liquid cells are still anticipated to show better capacity retention at elevated charge rates due to their significant pseudocapacitive contributions that amount to 75%.
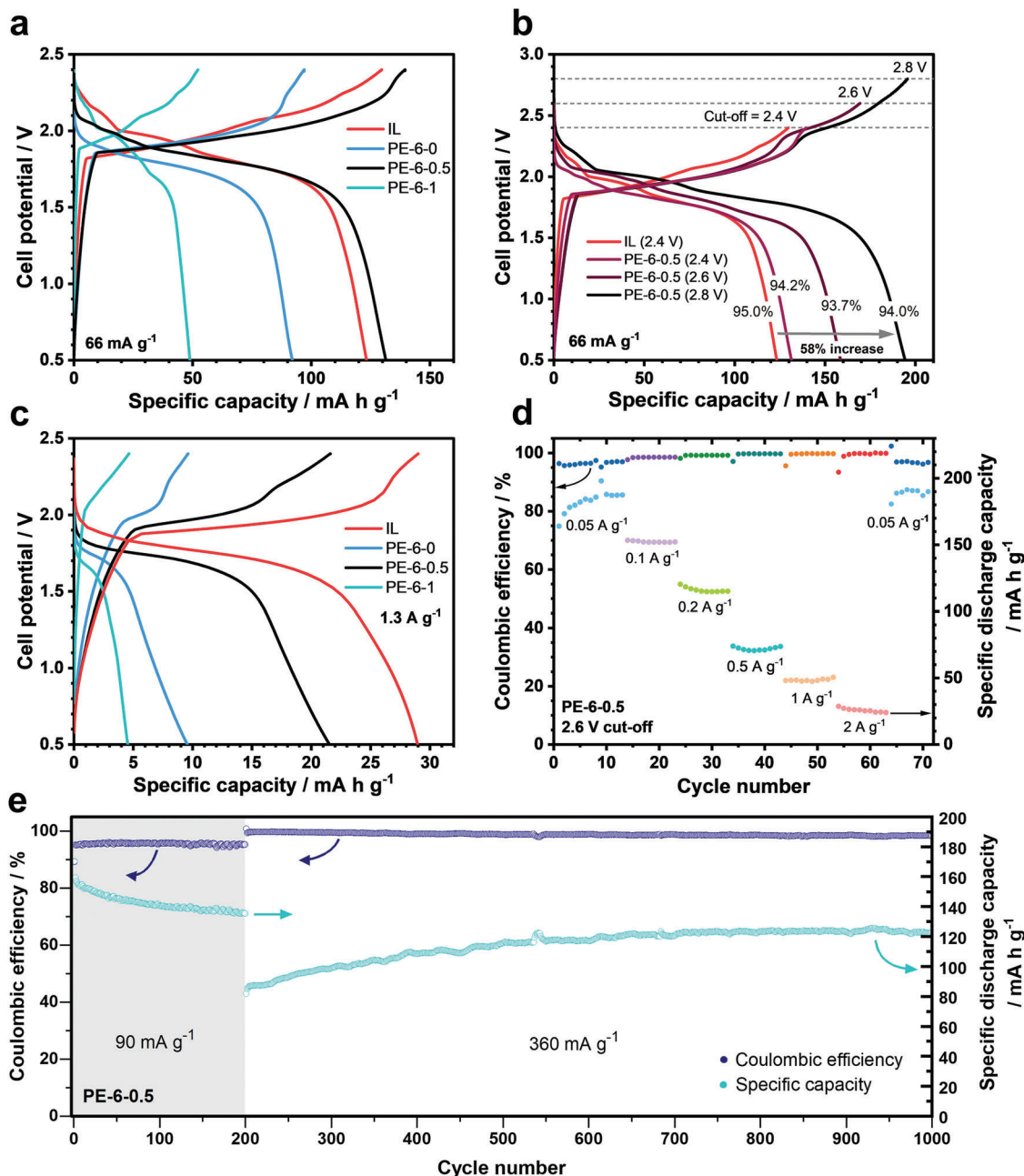
Figure 4. Charge-discharge curves of Al–natural graphite cells assembled with a) the ionic liquid (IL) and various polymer electrolytes, cycled at 66 mA g^{-1} to an upper cut-off potential of 2.4 V (fifth cycle), and b) the PE-6-0.5 electrolyte, cycled at 66 mA g^{-1} to upper cut-off potentials of 2.4, 2.6 and 2.8 V. c) Comparison of the specific capacities of cells with different electrolytes, cycled at a specific current of 1.3 A g^{-1}. Specific capacities and coulombic efficiencies of PE-6-0.5 Al–natural graphite cells, cycled at d) varying rates to 2.6 V, and e) 90 mA g^{-1} and 360 mA g^{-1} to a cut-off potential of 2.7 V for a total of 1000 cycles.

2.4. Electrolyte Performance in Al–Natural Graphite Batteries

The cycling characteristics of Al–natural graphite cells constructed using PE-6-0, PE-6-0.5, and PE-6-1 electrolytes were compared with cells assembled with the neat EMImCl-AlCl$_3$ ionic liquid (**Figure** 4a). At a 2.4 V charging cut-off potential, the ionic liquid cell exhibits a specific capacity of 123 mA h g^{-1} at 66 mA g^{-1}, similar to other reports in the literature.[9,17,48] The

PE-6-0.5 exhibits a slightly higher specific capacity than the ionic liquid when charged to 2.4 V (131 mA h g^{-1}), which is likely due to the thick glass fiber separator used to separate the positive and negative electrodes in the ionic liquid cell. Although similar volumes of electrolyte are used in each cell relative to the electrode area, the absorption of the ionic liquid into the thick, porous separator may restrict electrolyte utilization that consequently limits the availability of ions for charge storage and thus

the resulting capacity. The method of coating the graphite electrode with molten polymer electrolyte during cell assembly allows the polymer electrolyte, once solidified, to conform well to the electrode surface to create a stable interface. The PE-6-0 and PE-6-1 electrolytes show comparatively lower specific capacities due to a lower proportion of $Al_2Cl_7^-$ ions within the electrolyte as shown by the solid-state NMR studies, since increasing the molar ratio of $AlCl_3$:EMImCl, and thus Lewis acidity, of the ionic liquid typically results in higher specific capacities in Al–graphite batteries.[46,49]

Owing to the increased potential stability limits of the polymer electrolytes, the Al–natural graphite cells can be charged to higher potentials without significant detriment to the coulombic efficiency or electrolyte degradation. Figure 4b shows the charge and discharge characteristics of a cell constructed with the PE-6-0.5 electrolyte at upper cut-off potentials of 2.4, 2.6, and 2.8 V. The plateaus observed in the charge-discharge curves correspond well with the anodic and cathodic (de-)intercalation peaks present in the CV of the cell (Figure S10a, Supporting Information); peaks beyond 2.5 V that would indicate decomposition of the electrolyte were not observed. When galvanostatically cycled to 2.4 V at a specific current of 66 mA g^{-1}, a coulombic efficiency of 94.2% is achieved. Raising the cut-off potential to 2.6 V reduces the coulombic efficiency slightly by 0.5%, but yields a 21% increase in specific capacity, reaching 158 mA g^{-1}. At a 2.8 V cut-off potential, the coulombic efficiency is 94%, suggesting little to no additional decomposition of the electrolyte. For comparison, galvanically cycling an ionic liquid Al–graphite cell to 2.6 V gives a specific discharge capacity of 42 mA h g^{-1} and a coulombic efficiency of only 53% (Figure S10b, Supporting Information), due to the irreversible decomposition of the ionic liquid electrolyte at potentials above 2.45 V. Increasing the charging cut-off potential from 2.4 to 2.8 V unlocks a ≈48% increase in the specific capacity, reaching 194 mA h g^{-1} after three cycles at 2.8 V which is 58% higher than the ionic liquid and ca. 34% more than the highest capacity Al–graphite cells reported to date.[8]

Figure 4c shows the charge–discharge profiles of the Al–natural graphite cells at a high charge rate of 1.3 A g^{-1}. As expected, the cell assembled with the ionic liquid electrolyte exhibits the highest capacity retention at high charge rates, due to the significant pseudocapacitive contributions highlighted previously. The specific capacities of the PE-6-0 and PE-6-1 cells at 1.3 A g^{-1} both drop to ≈10% of their initial capacities at 66 mA g^{-1}, consistent with their lower pseudocapacitive charge storage. The reduced ion mobility in the polymer electrolytes causes a localized depletion of ions at the electrode surface during high charging rates, limiting the resulting specific capacities. Additionally, comparisons of EIS measurements of the Al–natural graphite cells reveal the presence of an additional semicircle in the mid-frequency region (between ca. 10 Hz and 3.3 kHz) of the polymer electrolytes as shown in the complex plane plots in Figure S11 (Supporting Information). This is ascribed to the solid-solid interface between the solid polymer electrolyte and the graphite electrode, which introduces an additional resistance that likely contributes to the reduced performance of the polymer electrolytes at high rates compared with the ionic liquid electrolyte at a 2.4 V charging cut-off potential, while potentially serving as a protective barrier to reduce polymer electrolyte degradation at higher potentials. The ionic liquid shows a lower

bulk resistance (1.6 Ω cm^2) than the polymer electrolytes (8.8–18 Ω cm^2), due to the thicker polymer electrolyte layer used to assemble the cells. The semicircle in the high-frequency region is attributed to the charge-transfer resistance between the electrolyte and graphite electrode.[50]

To demonstrate the significance of the enhanced potential stabilities of the polymer electrolyte, the cycling characteristics of PE-6-0.5 in an Al–graphite cell at charge rates between 50 mA g^{-1} and 2 A g^{-1} at an elevated cut-off potential of 2.6 V are presented in Figure 4d. The cell shows stable cycling behavior and reaches coulombic efficiencies of over 99% at charge rates above 200 mA g^{-1}. Importantly, the increased potential stability of the polymer electrolyte allows the cell to achieve specific capacities that are 20–55% higher than those of the ionic liquid Al–graphite cell, simply by raising the charging potential by 200 mV. The coulombic efficiencies achieved by the PE-6-0.5 electrolyte are also comparatively higher than those of the ionic liquid when charged to 2.4 V at the same rates. Charge–discharge curves and corresponding rate performance plots of the ionic liquid cell at various charge rates are provided in Figure S12a,b (Supporting Information) for comparison. Due to the typically reduced ionic mobilities in gel and solid polymer electrolytes, retaining high specific capacities at fast charge rates is challenging. However, the PE-6-0.5 electrolyte exhibits comparable rate performance to other Al polymer electrolytes recently reported in the literature,[10,11,27,39] attributed to its high ionic conductivity of 13.2 mS cm^{-1} enabled by the solid polymer network created by the cross-linking of PEO chains with a five-coordinate Al species, as discussed previously. Although the specific capacity of the cell decreases to 26 mA h g^{-1} at 2 A g^{-1}, this is still 30% higher than that of the ionic liquid cell (20 mA h g^{-1}). The original specific capacity of almost 190 mA h g^{-1} is recovered once the charge rate is decreased to 50 mA g^{-1} at the 64th cycle, indicating that no degradation or chemical damage has occurred as a result of cycling to elevated rates.

Long-term cycling of the PE-6-0.5 electrolyte to 2.7 V was performed over 1000 cycles (Figure 4e), initially at 90 mA g^{-1} for 200 cycles, followed by 800 cycles at 360 mA g^{-1}. Corresponding charge-discharge curves of selected cycles are shown in Figure S13 (Supporting Information). A specific capacity of 170 mA h g^{-1} was observed at the first cycle, with 89% coulombic efficiency. The relatively low coulombic efficiency and decrease in specific capacity during the initial cycles is attributed to the trapping of $AlCl_4^-$ ions between the graphene layers of the graphite electrode, as observed experimentally in natural graphite electrodes using solid-state ^{27}Al NMR spectroscopy.[1,17,51] Although the coulombic efficiency stabilizes at ≈95.5% after the first few cycles, a gradual decay in capacity is observed, attributed to the catalytic side reactions that occur at graphite defects. This is more pronounced at low charge rates, since faster charge rates introduce kinetic limitations that help suppress these side reactions,[1,17] resulting in a higher coulombic efficiency and longer cycling lifetime, accounting for the differences in the trends of the specific capacities observed in Figure 4e. Note that cycling to a slightly lower cut-off potential of 2.6 V resulted in higher coulombic efficiencies (97.0% at 50 mA g^{-1}, 98.6% at 100 mA g^{-1}, Figure 4d). Thus, if long-term cycling is the goal, then lower charging limits can be used to enhance cycle life. The PE-6-0.5 electrolyte further exhibits an average discharge

potential of 1.91 at the 2.7 V cut-off potential, which is 0.16 V higher than that of the ionic liquid when cycled at the same rate of 90 mA g^{-1}, but to a limit of 2.4 V. Increasing the discharge potential is crucial to achieving battery chemistries with increased specific energy and density.

Raising the specific current to 360 mA g^{-1} at the 201st cycle initially causes the specific capacity to drop to 82 mA h g^{-1}. The corresponding charge-discharge curve in Figure S13b (Supporting Information) shows significant polarization and an absence of charge and discharge plateaus in the 2.4–2.5 V region. However, continued cycling of the cell over the next 800 cycles reveals a gradual recovery of specific capacity, reaching 123 mA h g^{-1} at the 1000th cycle with 98.4% coulombic efficiency. The repeated AlCl$_4^-$ (de-)intercalation likely induces mild graphite exfoliation to enable easier access to intercalation sites, as evidenced by the re-emergence and increasing prominence of the charge and discharge plateaus at ca. 2.4 and 2.5 V over successive cycles (Figure S13b, Supporting Information). Ex situ SEM analysis of the Al electrode following long-term cycling reveals some surface pitting, but no evidence of dendrite formation (Figure S14, Supporting Information).

3. Conclusion

In this work, we present solid polymer electrolytes based on EMImCl-AlCl$_3$, PEO and fumed SiO$_2$ for applications in high-capacity Al–graphite batteries. The electrolytes exhibit increased electrochemical stability over the neat ionic liquid, allowing for charging cut-off potentials up to 2.8 V in Al–natural graphite cells. Charging to elevated potentials directly results in significantly increased cell discharge potentials and capacities, due to easier access to higher levels of graphite intercalation. Solid-state ^{27}Al single-pulse, multiple-quantum and dipolar-mediated ^{27}Al{^{1}H} NMR experiments revealed that Al$_2$Cl$_7^-$ anions react with ethylene oxide groups to form five-coordinate Al moieties that crosslink the PEO network and solidify the electrolyte. The resulting solid polymer matrix encapsulates a high proportion of ionic liquid to retain a high ionic conductivity of 13.2 mS cm^{-1}, despite being in a solid state. This lends itself to highly reversible cycling at current densities of up to 2 A g^{-1}. Solid-state ^{29}Si and ^{27}Al single-pulse NMR measurements also establish that the addition of fumed SiO$_2$ (<1 wt%) to the polymer electrolyte increases the Al$_2$Cl$_7^-$ content within the electrolyte due to a reaction between SiO$_2$ and AlCl$_4^-$ in the presence of PEO. The polymer electrolyte developed maintains coulombic efficiencies over 95% in Al–graphite cells at an elevated charging potential of 2.7 V for over 1000 cycles. Increased average discharge potentials of up to 1.91 V are also achieved with the polymer electrolyte, allowing for the development of batteries with higher specific energies. The results of this work unfold the unique synergistic effects of PEO and fumed SiO$_2$ in EMImCl-AlCl$_3$-based polymer electrolyte mixtures and provide a new approach toward developing solid-state electrolytes for high-performance Al batteries.

4. Experimental Section

Preparation of Polymer Electrolytes: Polymer electrolyte samples containing between 4 and 10 wt% PEO and up to 2.5 wt% SiO$_2$ were prepared in an argon-filled glove box (MBraun UNILab Pro; O$_2$ and H$_2$O ≤ 0.5 ppm) by combining PEO (Acros Organics, molecular weight = 100 000 g mol^{-1}) and fumed SiO$_2$ (Alfa Aesar, 325 mesh, 175–225 m^2 g^{-1} specific surface area) with the EMImCl-AlCl$_3$ ionic liquid (Sigma-Aldrich, AlCl$_3$/EMImCl molar ratio = 1.5).[12] The electrolyte mixtures were magnetically stirred in a sealed glass vessel at 375 rpm for 1 h at 80 °C until the PEO was completely dissolved, and a homogeneous mixture was formed. This melting step was followed by a 48-h period of cooling at room temperature to a gel-like state. The cycle of heating, stirring, and cooling was repeated twice more at the same conditions (80 °C, 375 rpm and 48-h cooling at 25 °C) for a total of three cycles. The electrolytes solidify after a period of rest from the third cycle onward and could be re-melted and cast into molds to prepare battery electrolyte discs. (Figure S15, Supporting Information).

To prepare samples for CV and EIS measurements, the solidified electrolytes were liquified at ≈80 °C and poured into 2.5 mm thick perfluoroalkoxy ring molds placed on top of a flat glass plate. The inner and outer diameters of the ring were 11 mm and 22 mm, respectively. An Al wire quasi-reference electrode (Alfa Aesar; 0.5 mm diameter, 99.999%) was inserted into the center of the electrolyte disc via a 1 mm diameter opening at the side of the ring (Figure S15, Supporting Information). The electrolytes were left to solidify for at least 24 h prior to electrochemical testing.

Electrochemical Measurements: All electrochemical measurements were performed in an inert argon atmosphere using a BioLogic SP-150 potentiostat at 25 °C. Variable-rate CVs of the Al electroplating and stripping behavior of the polymer electrolytes were recorded using a three-electrode cell with glassy carbon (Micro-to-Nano; high purity) working and counter electrodes and an Al wire (Alfa Aesar, 0.5 mm diameter, 99.999%) quasi-reference electrode. The three-electrode cell was assembled by placing the solid electrolyte disc, prepared as described above, between two glassy carbon disc electrodes secured by a plastic clamp (Figure S15b, Supporting Information). The distance between the electrodes was 2.5 mm, with an electrode–electrolyte contact surface area *A* of 0.95 cm^2. Potentiostatic EIS measurements were recorded using the same three-electrode cell from 500 kHz to 10 mHz at the open circuit potential using a sinusoidal amplitude of 10 mV. CV of the ionic liquid was recorded in a three-electrode cell using glassy carbon rods (3 mm diameter) as working and counter electrodes against an Al wire quasi-reference electrode, where the electrode surface area was taken as the area of the working electrode immersed in the ionic liquid.

Microscopic Characterization: SEM and EDX analyses of Al electrodeposits and the Al electrode following long-term cycling were performed using a JEOL JCM-6000 scanning electron microscope with a JEOL EX-230**BU EX-37001 EDX module. Al electrodeposits from the polymer electrolytes were obtained via constant-potential electrodeposition in a three-electrode cell on glassy carbon substrates, applying a constant potential of –0.3 V vs Al|Al(III) for 30 min at 25 °C. The samples were rinsed with dimethyl carbonate (99+%, extra dry, Acros Organics) to remove excess electrolyte residue prior to examination in the scanning electron microscope.

Graphite Electrode Preparation: A solution of 5 wt% polyvinylidene fluoride (PVDF) in *n*-methyl-2-pyrrolidinone (NMP) was first prepared by combining PVDF (Alfa Aesar) and NMP (Alfa Aesar, 99+%) under constant magnetic stirring for 12 h. Natural graphite powder (Alfa Aesar, 99.9995% purity) was added to the PVDF-NMP solution in a 1:2.22 mass ratio to yield an electrode slurry, which was stirred for 1 h until homogeneous. The slurry was cast onto a piece of 0.025 mm thick Mo foil current collector (Alfa Aesar, 99.95% purity) with a doctor blade set to 0.65 mm. The electrode film was dried under vacuum for 12 h at 120 °C to yield electrodes with an average mass loading of 5.1 mg cm^{-2}. Although several studies had reported the instability of PVDF in chloroaluminate ionic liquids,[25,52,53] obvious degradation of the graphite electrode was not observed within the timescales of the experiments in this study (2–3 months).

Assembly and Electrochemical Measurements of Al–Graphite Cells: Natural graphite and Al foil (Alfa Aesar, 0.1 mm thick, 99.99% purity) electrodes were cut into 6 mm diameter circular discs. Al–graphite cells with polymer electrolytes were assembled directly in polytetrafluoroethylene (PTFE) Swagelok cells. Molten polymer electrolytes were cast directly onto

the graphite electrodes, using a 1 mm thick polypropylene spacer (5 mm inner diameter, 6 mm outer diameter) to hold the electrolyte in place. The Al electrode was placed on top of the cathode and electrolyte, and the cell was left for a minimum of 24 h to allow the electrolyte to re-solidify. Specific capacities and specific charge-discharge currents of the polymer electrolyte cells were normalized against the mass of graphite within the 5 mm diameter inner area of the polypropylene spacer (area = 0.196 cm^2). For cells assembled with the ionic liquid, a glass fiber separator (Whatman GF/D) was saturated with ionic liquid and placed between the Al and graphite electrodes. The Al–graphite cells were placed in the center of a PTFE Swagelok union and pressed together with molybdenum current collector rods (Alfa Aesar, 99.95% purity) for electrochemical testing. A schematic diagram of the Swagelok cell assembly is provided in Figure S16 (Supporting Information).

Galvanostatic cycling measurements of the Al–graphite battery cells were performed with upper cut-off limits ranging between 2.4 and 2.8 V, and a lower cut-off potential of 0.5 V. The cells were cycled at various charge rates from 50 mA g^{-1} to 2 A g^{-1}. Variable-rate CV measurements of the battery cells were obtained between cell potentials of 0.5 and 2.4 V, at scan rates from 0.1 to 1.0 mV s^{-1}. Galvanostatic EIS measurements were performed on Al–graphite cells at 0 mA with an applied sinusoidal amplitude of 100 μA between a frequency range of 500 kHz and 10 mHz. The cells were cycled galvanostatically for five cycles at 100 mA g^{-1} between 0.5 and 2.4 V prior to the EIS measurements. All electrochemical measurements were performed at 25 °C.

Solid-State NMR Spectroscopy: Solid-state NMR spectra were acquired on a Bruker AVANCE III HD 600 NMR spectrometer with a 14.1 T narrow-bore (54 mm diameter) superconducting magnet operating at 600.140 MHz for ^{1}H, 156.378 MHz for ^{27}Al, and 119.224 MHz for ^{29}Si nuclei, respectively. A Phoenix NMR 1.6 mm HXY MAS probehead was used, where all measurements were conducted at 40 kHz MAS. Air was pumped through the probehead at 600 L h^{-1} and 298.1 K to mitigate MAS-induced sample heating.

^{27}Al radiofrequency (rf) pulses were calibrated on 1 M aqueous Al(NO$_3$)$_3$, where an rf field strength of 135 kHz (π/2 of 1.85 μs) was used for all broadband pulses. Solid-state ^{27}Al single-pulse MAS NMR experiments were performed under quantitative conditions by using (*i*) short π/12 rf pulses (0.308 μs) to ensure linear excitation[54,55] of all ^{27}Al signals (spin = 5/2), and (*ii*) recycle delays (0.05 s) such that all ^{27}Al nuclear spins were relaxed to thermal equilibrium (>5 × T_1). The 1D and 2D ^{27}Al{^{1}H} D-HMQC experiments were performed using the SR4$^2_1$ symmetry-based recoupling scheme[56,57] with a 450 μs recoupling time. The SR4$^2_1$ sequence recouples ^{27}Al–^{1}H dipolar interactions while simultaneously decoupling ^{1}H–^{1}H homonuclear interactions. Central-transition-selective pulses used a ^{27}Al rf field strength of 7.8 kHz (π/2 of 32 μs). SR4$^2_1$ recoupling pulses used a ^{1}H rf field strength of 80 kHz (2 × MAS frequency). Preparatory, diverging ^{27}Al double-frequency sweep pulses were used to achieve up to three-fold signal enhancements. Double-frequency sweep pulses were swept from 50 kHz to 1 MHz prior to each scan. 2D ^{27}Al{^{27}Al} MQ-MAS experiments were performed using a three-pulse sequence with excitation and conversion rf pulses of 3.2 and 1.1 μs, respectively, a central-transition-selective π/2 readout pulse of 32 μs, and a *z*-filter delay of 25 μs. Triple-quantum to single-quantum coherence selection was obtained via phase cycling.

Solid-state ^{29}Si single-pulse NMR experiments used an rf field strength of 125 kHz (π/2 of 2.00 μs) for all broadband pulses. All solid-state ^{27}Al single-pulse and ^{27}Al{^{1}H} D-HMQC NMR measurements, as well as the ^{29}Si single-pulse measurements, were acquired under ^{1}H heteronuclear decoupling using the SPINAL-64 pulse scheme with a ^{1}H rf field strength of 100 kHz. ^{27}Al shifts were referenced to a 1 M aqueous Al(NO$_3$)$_3$ solution at 0 ppm. ^{1}H and ^{29}Si shifts were referenced with respect to tetramethylsilane at 0 ppm by using adamantane and tetrakis(trimethylsilyl)silane as secondary chemical shift references, respectively.

Density Functional Theory Calculations: DFT calculations were performed on five-coordinate Al complexes containing differing combinations of chlorine and oxygen ligands. The molecular clusters were built using the Avogadro Molecular Editor software[58,59] and first optimized using the universal force field. DFT calculations to understand the NMR parameters of these molecular clusters were performed in Gaussian 09[60] using the 6–31G+(d,p) basis set and hybrid B3LYP method (Becke's three-parameter non-local exchange functional and Lee–Yang–Parr's correlation functional). Gauge-independent atomic orbital calculations yielded chemical shielding values and the eigenvalues of the electric field gradient tensors. The electric field gradient eigenvalues were arranged such that $|V_{xx}|<|V_{yy}|<|V_{zz}|$, and the quadrupolar coupling constants (C_Q), quadrupolar asymmetry parameters (η_Q), and 2nd order quadrupolar shifts were calculated from these values.[4,51]

Supporting Information

Supporting Information is available from the Wiley Online Library or from the author.

Conflict of Interest

The authors declare no conflict of interest.

Data Availability Statement

The data that support the findings of this study are available from the corresponding author upon reasonable request.

[1] G. A. Elia, I. Hasa, G. Greco, T. Diemant, K. Marquardt, K. Hoeppner, R. J. Behm, A. Hoell, S. Passerini, R. Hahn, *J. Mater. Chem. A* **2017**, *5*, 9682.

[2] Y. Song, S. Jiao, J. Tu, J. Wang, Y. Liu, H. Jiao, X. Mao, Z. Guo, D. J. Fray, *J. Mater. Chem. A* **2017**, *5*, 1282.

[3] M. Angell, G. Zhu, M.-C. Lin, Y. Rong, H. Dai, *Adv. Funct. Mater.* **2019**, *30*, 1901928.

[4] L. W. Gordon, J. Wang, R. J. Messinger, *J. Magn. Reson.* **2023**, *348*, 107374.

[5] A. Zhou, L. Jiang, J. Yue, Y. Tong, Q. Zhang, Z. Lin, B. Liu, C. Wu, L. Suo, Y.-S. Hu, H. Li, L. Chen, *ACS Appl. Mater. Interfaces* **2019**, *11*, 41356.

[6] W. Pan, Y. Wang, Y. Zhang, H. Y. H. Kwok, M. Wu, X. Zhao, D. Y. C. Leung, *J. Mater. Chem. A* **2019**, *7*, 17420.

[7] M.-C. Lin, M. Gong, B. Lu, Y. Wu, D.-Y. Wang, M. Guan, M. Angell, C. Chen, J. Yang, B.-J. Hwang, H. Dai, *Nature* **2015**, *520*, 324.

[8] S. Wang, K. V. Kravchyk, F. Krumeich, M. V. Kovalenko, *ACS Appl. Mater. Interfaces* **2017**, *9*, 28478.

[9] K. V. Kravchyk, S. Wang, L. Piveteau, M. V. Kovalenko, *Chem. Mater.* **2017**, *29*, 4484.

[10] A. Mohammad, T. Köhler, S. Biswas, H. Stöcker, D. C. Meyer, *ACS Appl. Energy Mater.* **2023**, *6*, 2914.

[11] I. Kim, S. Jang, K. H. Lee, Y. Tak, G. Lee, *Energy Storage Mater.* **2021**, *40*, 229.

[12] T. Schoetz, O. Leung, I. Efimov, C. Zaleski, Á. M. Ortega, N. G. García, P. Tiemblo Magro, C. Ponce de Leon, *J. Electrochem. Soc.* **2020**, *167*, 040516.

[13] X.-G. Sun, Y. Fang, X. Jiang, K. Yoshii, T. Tsuda, S. Dai, *Chem. Commun.* **2016**, *52*, 292.

[14] O. M. Leung, T. Schoetz, T. Prodromakis, C. Ponce De Leon, *J. Electrochem. Soc.* **2021**, *168*, 056509.

[15] J. H. Xu, T. Schoetz, J. R. Mcmanus, V. R. Subramanian, P. W. Fields, R. J. Messinger, *J. Electrochem. Soc.* **2021**, *168*, 060514.

[16] C.-Y. Chen, T. Tsuda, S. Kuwabata, C. L. Hussey, *Chem. Commun.* **2018**, *54*, 4164.

[17] J. H. Xu, D. E. Turney, A. L. Jadhav, R. J. Messinger, *ACS Appl. Energy Mater.* **2019**, *2*, 7799.

[18] Z. Yu, S. Jiao, J. Tu, W.-L. Song, H. Lei, H. Jiao, H. Chen, D. Fang, *J. Mater. Chem. A* **2019**, *7*, 20348.

[19] Z. Yu, S. Jiao, S. Li, X. Chen, W.-L. Song, T. Teng, J. Tu, H.-S. Chen, G. Zhang, D.-N. Fang, *Adv. Funct. Mater.* **2019**, *29*, 1806799.

[20] Z. Shui, Y. Chen, W. Zhao, X. Chen, *Langmuir* **2022**, *38*, 10791.

[21] J. D. Ortiz-Gonzalez, C. I. Sánchez-Sáenz, *ECS Trans.* **2021**, *100*, 73.

[22] Á. Miguel, N. García, V. Gregorio, A. López-Cudero, P. Tiemblo, *Polymers* **2020**, *12*, 1336.

[23] X. Shen, T. Sun, Z. Wu, L. Tan, *J. Mater. Chem. A* **2022**, *10*, 8178.

[24] S. Song, M. Kotobuki, F. Zheng, Q. Li, C. Xu, Y. Wang, W. D. Z. Li, N. Hu, L. Lu, *Solid State Ion* **2017**, *300*, 165.

[25] H. Wang, Y. Bai, S. Chen, X. Luo, C. Wu, F. Wu, J. Lu, K. Amine, *ACS Appl. Mater. Interfaces* **2015**, *7*, 80.

[26] Z. Yu, Z. Xie, W. Wang, J. Hong, J. Ge, *Frontiers in Chemistry* **2023**, *11*, https://doi.org/10.3389/fchem.2023.1190102.

[27] S. Zhang, Z. Liu, R. Liu, L. Du, L. Zheng, Z. Liu, K. Li, M.-C. Lin, Y. Bian, M. Cai, H. Du, *J. Power Sources* **2023**, *575*, 233110.

[28] Z. Liu, H. Du, Y. Cui, L. Du, Z. Zhao, X. Wang, Z. Lv, M. Sun, Z. Liu, K. Li, G. Zhang, M.-C. Lin, G. Cui, *J. Power Sources* **2021**, *497*, 229839.

[29] Y. Wang, W.-H. Zhong, *ChemElectroChem* **2015**, *2*, 22.

[30] J. Lopez, D. G. Mackanic, Y. Cui, Z. Bao, *Nat. Rev. Mater.* **2019**, *4*, 312.

[31] H. Zhao, J. Xu, D. Yin, Y. Du, *Chem. - Eur. J.* **2018**, *24*, 18220.

[32] M. P. S. Mousavi, A. J. Dittmer, B. E. Wilson, J. Hu, A. Stein, P. Bühlmann, *J. Electrochem. Soc.* **2015**, *162*, A2250.

[33] H. Wang, S. Gu, Y. Bai, S. Chen, N. Zhu, C. Wu, F. Wu, *J. Mater. Chem. A* **2015**, *3*, 22677.

[34] P. R. Gifford, J. B. Palmisano, *J. Electrochem. Soc.* **1987**, *134*, 610.

[35] K. V. Kravchyk, M. V. Kovalenko, *Commun. Chem.* **2020**, *3*, 120.

[36] B. Vestergaard, N. J. Bjerrum, I. Petrushina, H. A. Hjuler, R. W. Berg, M. Begtrup, *J. Electrochem. Soc.* **1993**, *140*, 3108.

[37] C. Ferrara, V. Dall'asta, V. Berbenni, E. Quartarone, P. Mustarelli, *J. Phys. Chem. C* **2017**, *121*, 26607.

[38] A. A. Fannin, D. A. Floreani, L. A. King, J. S. Landers, B. J. Piersma, D. J. Stech, R. L. Vaughn, J. S. Wilkes, J. L. Williams, *J. Phys. Chem.* **1984**, *88*, 2614.

[39] G. A. Elia, C. I. Acevedo, R. Kazemi, S. Fantini, R. Lin, R. Hahn, *Energy Technol.* **2021**, *9*, 2100208.

[40] Á. Miguel, P. Jankowski, J. L. Pablos, T. Corrales, A. López-Cudero, A. Bhowmik, D. Carrasco-Busturia, G. Ellis, N. García, J. M. García-Lastra, P. Tiemblo, *Polymer* **2021**, *224*, 123707.

[41] T. Schoetz, L. W. Gordon, S. Ivanov, A. Bund, D. Mandler, R. J. Messinger, *Electrochim. Acta* **2022**, *412*, 140072.

[42] Y. Long, H. Li, M. Ye, Z. Chen, Z. Wang, Y. Tao, Z. Weng, S.-Z. Qiao, Q.-H. Yang, *Energy Storage Mater.* **2021**, *34*, 194.

[43] D. Massiot, F. Fayon, M. Capron, I. King, S. Le Calvé, B. Alonso, J.-O. Durand, B. Bujoli, Z. Gan, G. Hoatson, *Magn. Reson. Chem.* **2002**, *40*, 70.

[44] Á. Miguel, R. P. Fornari, N. García, A. Bhowmik, D. Carrasco-Busturia, J. M. García-Lastra, P. Tiemblo, *ChemSusChem* **2020**, *13*, 5523.

[45] D. Lin, W. Liu, Y. Liu, H. R. Lee, P.-C. Hsu, K. Liu, Y. Cui, *Nano Lett.* **2016**, *16*, 459.

[46] K. V. Kravchyk, C. Seno, M. V. Kovalenko, *ACS Energy Lett.* **2020**, *5*, 545.

[47] K. V. Kravchyk, M. V. Kovalenko, *Adv. Energy Mater.* **2019**, *9*, 1901749.

[48] D.-Y. Wang, C.-Y. Wei, M.-C. Lin, C.-J. Pan, H.-L. Chou, H.-A. Chen, M. Gong, Y. Wu, C. Yuan, M. Angell, Y.-J. Hsieh, Y.-H. Chen, C.-Y. Wen, C.-W. Chen, B.-J. Hwang, C.-C. Chen, H. Dai, *Nat. Commun.* **2017**, *8*, 14283.

[49] T. Schoetz, J. H. Xu, R. J. Messinger, *ACS Appl. Energy Mater.* **2023**, *6*, 2845.

[50] S. Wang, Z. Yu, J. Tu, J. Wang, D. Tian, Y. Liu, S. Jiao, *Adv. Energy Mater.* **2016**, *6*, 1600137.

[51] J. H. Xu, A. L. Jadhav, D. E. Turney, R. J. Messinger, *J. Mater. Chem. A* **2020**, *8*, 16006.

[52] L. Geng, J. P. Scheifers, C. Fu, J. Zhang, B. P. T. Fokwa, J. Guo, *ACS Appl. Mater. Interfaces* **2017**, *9*, 21251.

[53] Y. Uemura, C.-Y. Chen, Y. Hashimoto, T. Tsuda, H. Matsumoto, S. Kuwabata, *ACS Appl. Energy Mater.* **2018**, *1*, 2269.

[54] D. Fenzke, D. Freude, T. Fröhlich, J. Haase, *Chem. Phys. Lett.* **1984**, *111*, 171.

[55] A. Samoson, E. Lippmaa, *Phys. Rev. B* **1983**, *28*, 6567.

[56] A. Brinkmann, A. P. M. Kentgens, *J. Am. Chem. Soc.* **2006**, *128*, 14758.

[57] M. H. Levitt, *Encyclopedia of Magnetic Resonance*, John Wiley & Sons, Ltd., Chichester, UK **2007**.

[58] AvogadroChemistry Avogadro: an open-source molecular builder and visualization tool. Version 1.2.0, **2016**.

[59] M. D. Hanwell, D. E. Curtis, D. C. Lonie, T. Vandermeersch, E. Zurek, G. R. Hutchison, *J. Cheminform.* **2012**, *4*, 17.

[60] M. J. Frisch, G. W. Trucks, H. B. Schlegel, G. E. Scuseria, M. A. Robb, J. R. Cheeseman, G. Scalmani, V. Barone, B. Mennucci, G. A. Petersson, H. Nakatsuji, M. Caricato, X. Li, H. P. Hratchian, A. F. Izmaylov, J. Bloino, G. Zheng, J. L. Sonnenberg, M. Hada, M. Ehara, K. Toyota, R. Fukuda, J. Hasegawa, M. Ishida, T. Nakajima, Y. Honda, O. Kitao, H. Nakai, T. Vreven, J. A. Montgomery Jr., et al. Gaussian 09 Revision E.01, Wallingford, CT, **2009**.